INTERNATIONAL ATOMIC ENERGY AGENCY
UNITED NATIONS EDUCATIONAL, SCIENTIFIC AND CULTURAL ORGANIZATION

INTERNATIONAL CENTRE FOR THEORETICAL PHYSICS
34100 TRIESTE (ITALY) - P.O.B. 586 - MIRAMARE - STRADA COSTIERA 11 - TELEPHONE: 2240-1
CABLE: CENTRATOM - TELEX 460392 - I

H4.SMR/222 - 21

SECOND AUTUMN WORKSHOP ON
CLOUD PHYSICS AND CLIMATE

(23 November - 18 December 1987)

# CLOUD AND PRECIPITATION PROCESSES

## Part IV

## Microphysics of deep convective clouds

G.VALI
University of Wyoming
U.S.A.

Workshop in Cloud Physics and Climate

23 November - 18 December 1987

CLOUD AND PRECIPITATION PROCESSES

Gabor Vali
University of Wyoming
U.S.A.

Part IV. Microphysics of deep convective clouds.

## IV. MICROPHYSICS OF DEEP CONVECTIVE CLOUDS

### a. FLORIDA

Mesoscale convergence over the peninsula - convergence lines near coasts IV/1-3

Deep convection and heavy precipitation associated with convergence

<u>Microphysics studied by aircraft</u>

Repeated penetrations between -5 and -9°C levels IV/4-5

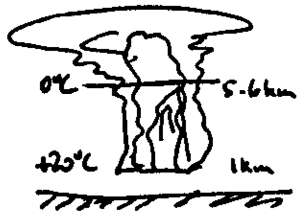


1. New towers have no ice (<0.1/lit)
2. Within 5 minutes >10/lit graupel present; not correlated with updraft or with LWC
3. Cloud droplets >25 μm dia present Rain drops >0.5 mm present
4. Vapor-grown crystals observed at times

<u>Process:</u> IV/6-8

Proto-ice rimes with cloud droplets -> splinters (H-M) produced -> splinters collected by supercooled raindrops; freeze -> graupel grows by further riming -> more splinters produced, providing positive feedback

Graupel falls out and melts at lower levels

Origin of proto-ice unknown

Multiplication by 100 possible in 5 minutes

<u>Radar echo studies:</u> IV/9

Individual cells tracked by objective routine
Correlations between echo height and other parameters

Numerical models:

3D model with parameterized microphysics IV/10

Seeding experiments

Florida Area Cumulus Experiment (FACE) I and II

Hypothesis - dynamic seeding effect IV/11

Physical evidence - growth observed, modeled IV/12
- more ice observed
- propagation of effect from bouyancy aloft to increased moisture flux at base not explained
- secondary ice production competes with seeding

Statistical evidence - positive, but not statistically significant

b. HIGH PLAINS

North-central U.S.; East of Rocky Mountains
Summertime rainfall is low, from convective clouds; hailstorms frequent
Cool dry air at surface - high cloud bases, +5 to 0°C
Continental airmasses - narrow cloud droplet spectra

Evidence for precipition development via graupel growth:

* First echoes at ~ -12°C
* No supercooled drops >100 μm observed
* Precipitqation-sized (>500 μm) particles are rimed crystals
* Non-rimed crystals form at T < -15°C in concentrations of >1 per liter, often reaching >100 per liter
* Time of echo formation coincides with in-situ observation of small graupel

Inflow and updraft structure

High $\theta_E$ air from near surface (usually SE) IV/13



Updrafts of moderate magnitude, negative bouyancy at cloud base and slightly above IV/14
Not much increase with altidude; values to 20 m s$^{-1}$ IV/15

Microphysics

Liquid water contents usually less than 1 g m$^{-3}$ IV/16
Much below adiabatic values IV/17-19

Droplet concentrations 600-1000 cm$^{-3}$ IV/20

Ice particle concentrations IV/21
Example of graupel development IV/22

HIPLEX seeding experiment

Small *Cu con* (tops -12 to -15°C) seeded at ~ -10°C IV/23

Seeding effect observed, as hypothesized until ~ 8 min. IV/24-25

Decay of liquid water content is faster than needed for graupel growth and precipitation development IV/26

IV/1

PIELKE, 1974
Mo Wea Rev. p115

FIG. 18. Gemini photograph of south Florida taken 5 June 1966 at 1251 EST looking southwest. (Photograph courtesy of NASA.)

IV/2

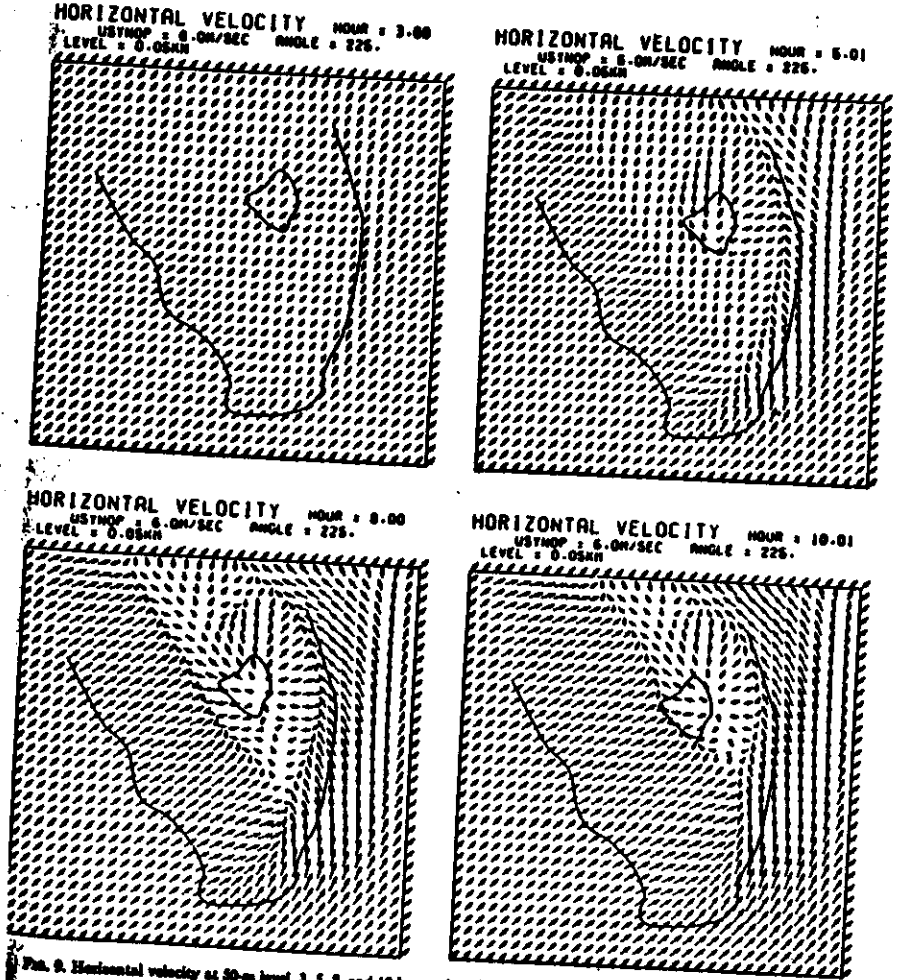


FIG. 9. Horizontal velocity at 50-m level, 3, 5, 8, and 10 hours after simulated sunrise for the synoptic southwest wind case.

IV/3



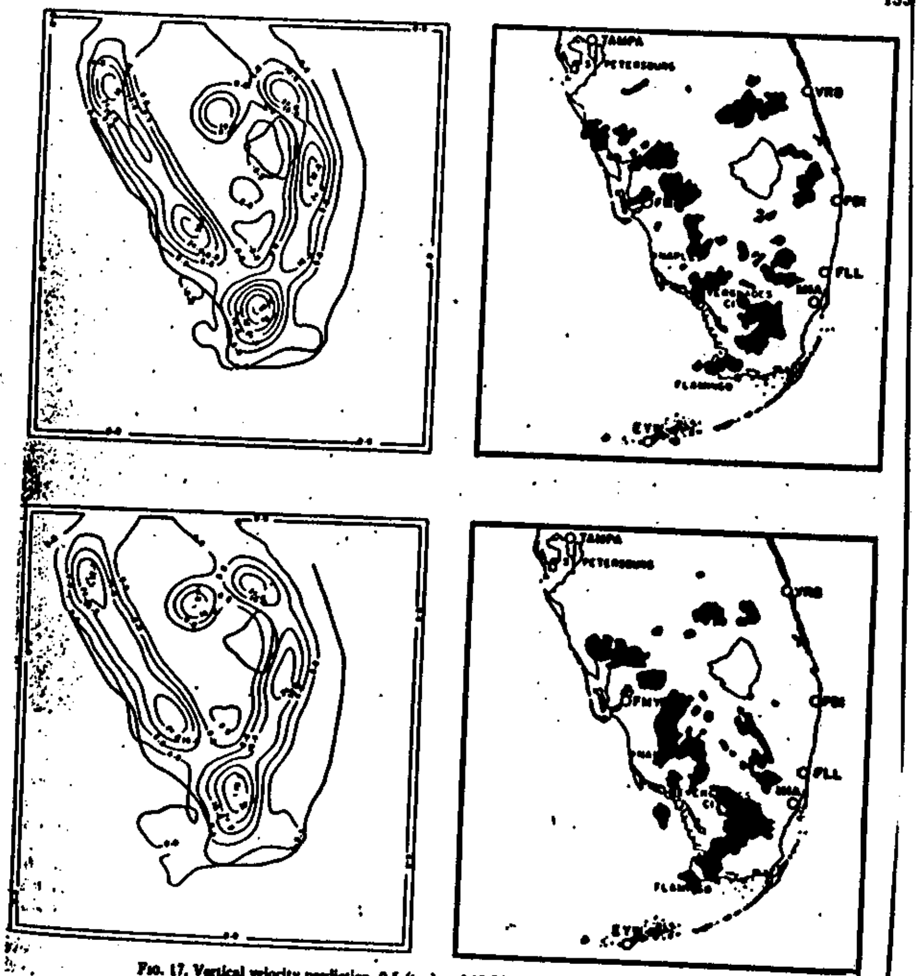


FIG. 17. Vertical velocity prediction, 9.5 (top) and 10.5 hours after simulated sunrise, and composite radar maps at equivalent times for 29 June 1971.

IV/4

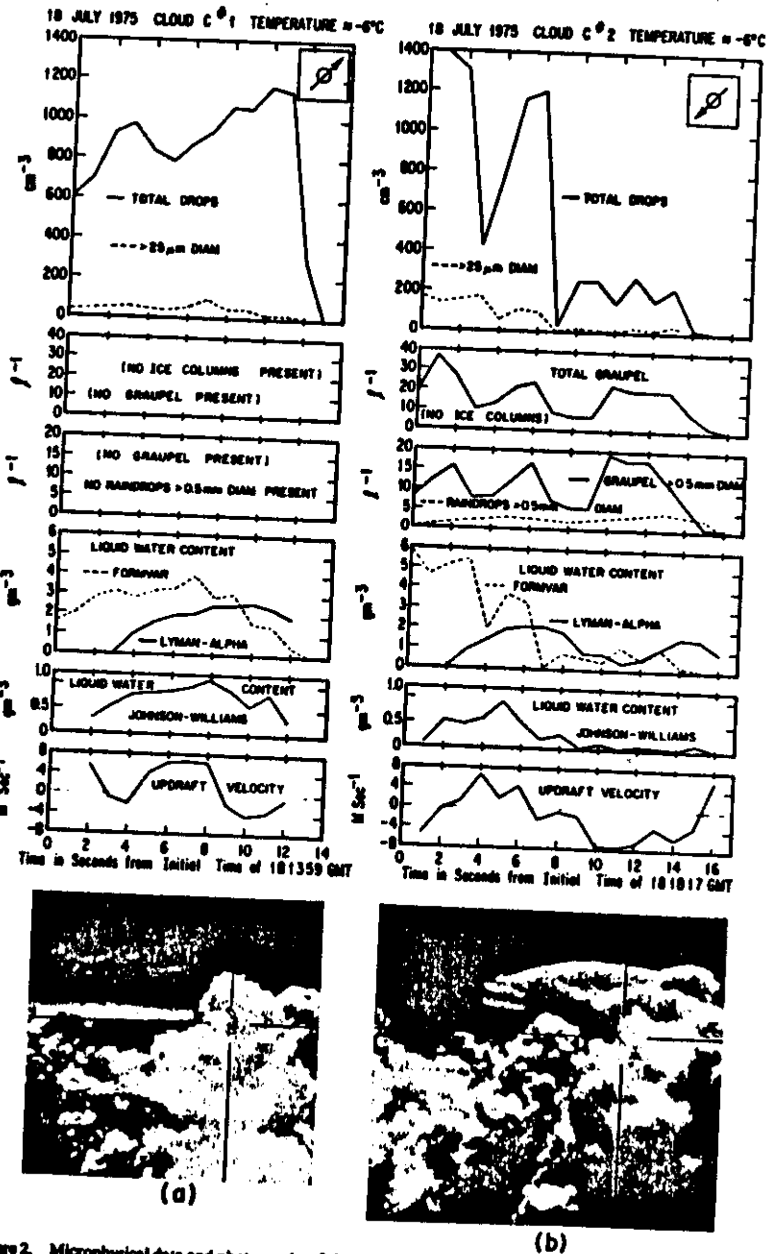


Figure 2. Microphysical data and photographs of cloud C on 18 July 1975. (a) Pass 1; (b) Pass 2. The boxed arrow in the upper right corner of each data set indicates the heading of the aircraft during penetration (north toward top). 10 s represents approximately a 1 km path.

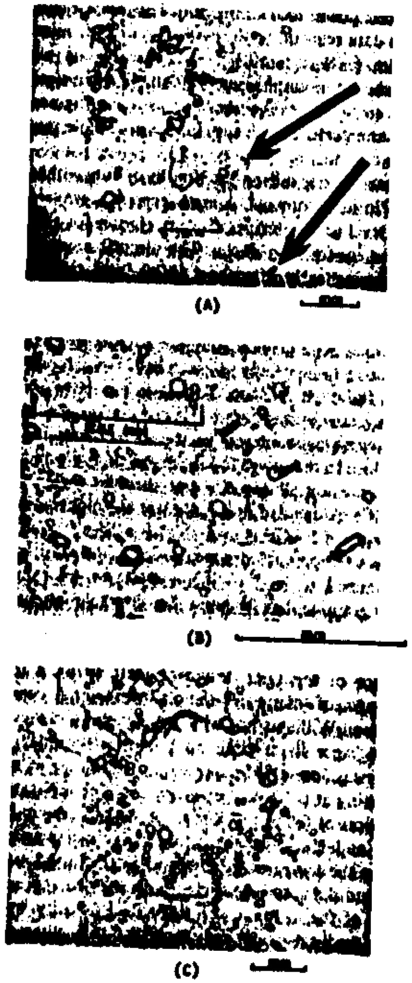


Figure 1. Examples of formvar replica from pass B1 on 27 July 1975. (a) Fragments from a graupel particle that impacted in the upper left quarter of the frame and vapour-grown ice columns (arrows); (b) Expanded view of the columns shown in (a); (c) Characteristic splash pattern from a large liquid drop. The diameter of the original drop was ~0·2 times the splash diameter.

separate from graupel impact craters (see Fig. 1(a), arrows). No irregular ice fragments were considered in this analysis, the tendency being toward strong conservatism in classifying columns. If any doubt existed, the ice was considered as a fragment (resulting from a

graupe
of the
been l
substr
a crite
patter
temper

A
by the
contai
observ
were a
of the
the cl
12 occ
diamet
in all c
per-pe
(±5μ
impact
descrip
noted t
nature
0·75%
~400-
concen
the cas
3 min,
Th
present
twice w
(north
carried
determi
level of
near 1
−9°C
appear
that th
(≈300
peaked
the dro
above 3
of clou
the wat
is abou

IV/5

IV/6

HALLETT et al 1978; QJRMS p 631
LAMB, HALLETT 1981; QJRMS p 935

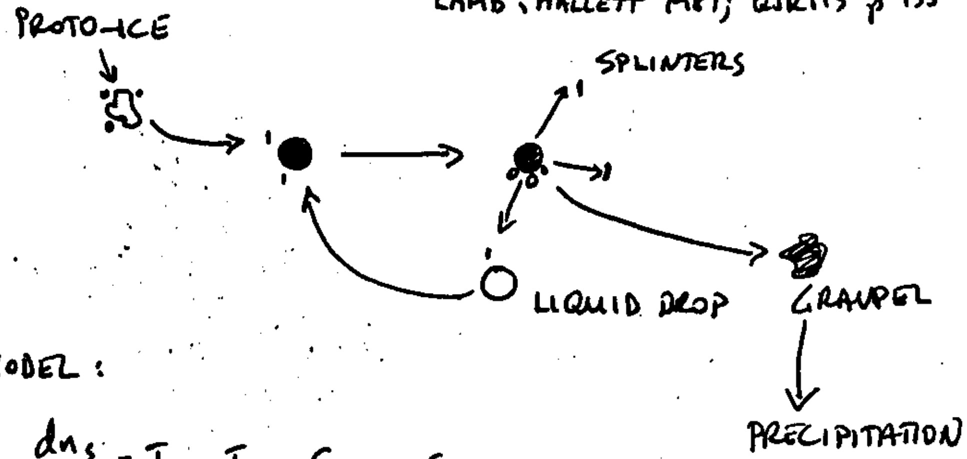


MODEL:

$$\frac{dn_s}{dt} = J_s - J_{dl} = S_g n_g - S_{dl} n_s$$

$$\frac{dn_g}{dt} = J_{dl}$$

$n_s$ – concentration of splinters
$n_g$ – " of graupel
$n_{dl}$ – " of drops

$S_{dl} = n_{dl} \pi r_{dl}^2 v_{dl} E_{dl}$ – sweep-out by drops

$S_g = n_{25} \alpha \pi r_g^2 v_g E_g$ – production per graupel

$n_{25}$ – concentration of droplets $>25\,\mu m$

$\alpha$ – splinter production efficiency

$\frac{1}{S_{dl}} = \tau_r$ time constant for removal

$\frac{1}{S_g} = \tau_p$ time constant for production.

$\alpha = 0.005 - 0.02$

HALLETT et al 1978 IV/7



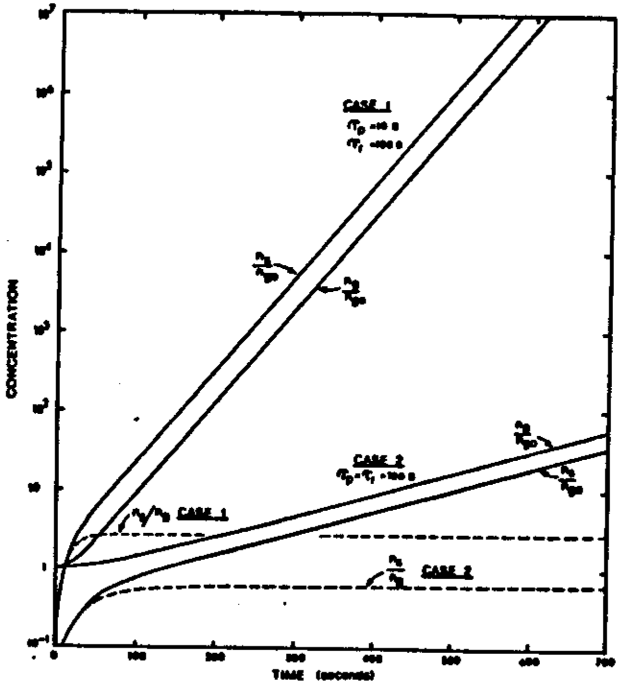


gure 7. The evolution with time of the number concentrations of secondary splinters ($n_s$) and graupel ($n_g$) r two cases of the conceptual model (see text). $\tau_p$ represents the time constant for splinter production, $\tau_r$ that for removal of the splinters by supercooled drops.

graupel is thus seen to approach a constant value in each case, depending upon the spective time constants. Particularly noteworthy is that multiplication factors of $O(10^3)$ ise in times less than five minutes in case 1, the case with the higher splinter production te. Although the basic trends shown in Fig. 7 are intuitively reasonable, it is well cognized that the assumptions, primarily of constant $S_g$ and $S_{dl}$, impose limitations ich prohibit direct application of this simple conceptual model to the real atmosphere. evertheless, the concept of 'in situ' multiplication based on the scavenging of secondary linters by large supercooled drops is seen to be potentially powerful and could well be basis for the actual multiplication of graupel in Florida cumuli. This further implies at the evolution of the ice phase in such clouds in general depends intimately upon the ior and independent evolution of the liquid phase.

It should be noted that weak to moderate updraught speeds (up to several metres r second) are favoured for the optimum conversion of liquid water drops to new graupel

IV/8

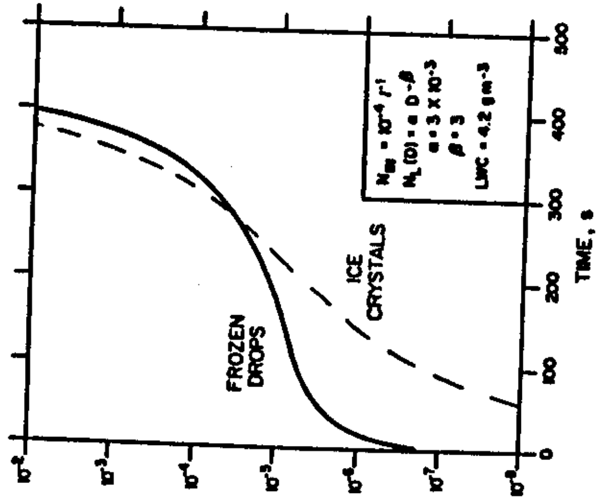


Fig. 2. Model output of the evolution of ice for the case of a high raindrop concentration.

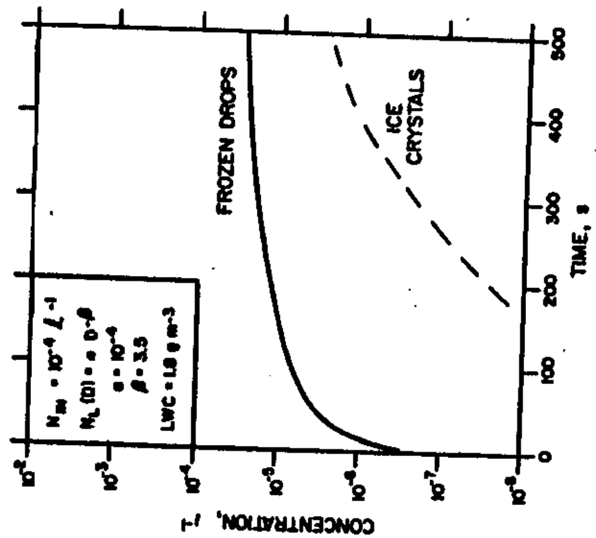


Fig. 3. Model output of the evolution of ice for the case of a reduced concentration of raindrops.

## VI REFERENCES

Foster, T and J. Hallett, 1982: A laboratory investigation of the influence of liquid water content on the temperature dependence of secondary ice production during soft hail growth. Proceedings of Conference on Cloud Physics, Chicago, Nov. 1982.

-llett, J., and S.C. Mossop, 1974: Production of secondary ice particles during the riming pro-

Lamb, D., J. Hallett and R.I. Sax, 1981: Mechanistic limitations to the release of latent heat during the natural and artificial glaciation of deep convective clouds. Q. J. Roy. Meteor. Soc., 107, 935-954.

Locatelli, J.D. and P.V. Hobbs, 1974: Fall speeds and masses of solid precipitation particles. J. Geophys. Res., 79, 2185-2197.

Mossop, S.C., 1978: The influence of drop size distri-

GAGIN et al. 1985 J. Atm. Sci. p88

IV/

TRIPOLI, COTTON, 1980 J. Appl. Meteor p103

IV/11

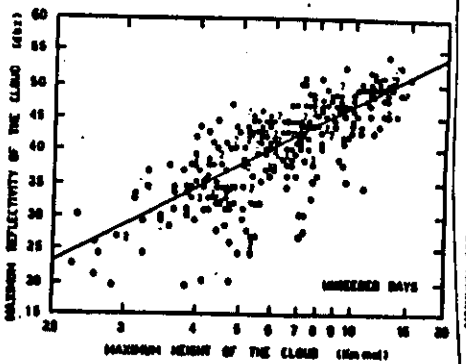


FIG. 5. The relationship between lifetime maximum cell reflectivity $dBz_{max}$ and the factor $(H_{max} - h)$ defined by the lifetime maximum height $H_{max}$ of the cells.

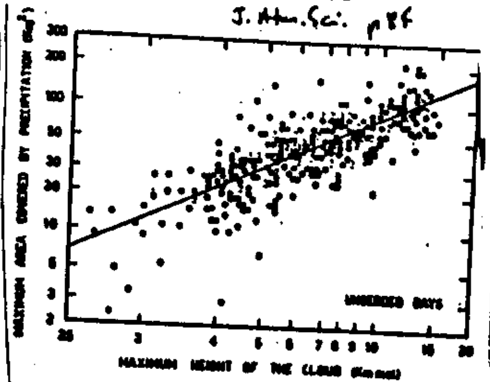


FIG. 6. As in Fig. 5 but for the lifetime maximum area $A_{max}$ covered by the cell precipitation and $H_{max} - h$.

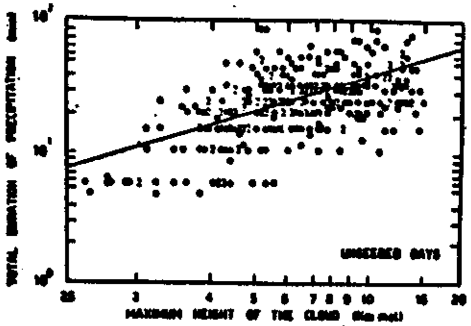


FIG. 7. As in Fig. 5. but for the total duration of precipitation DUR and $H_{max} - h$.

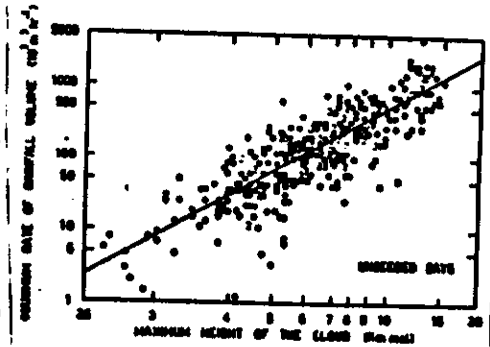


FIG. 8. As in Fig. 5 but for the lifetime maximum of total rainfall volume rate $RVR_{max}$ and $H_{max} - h$.

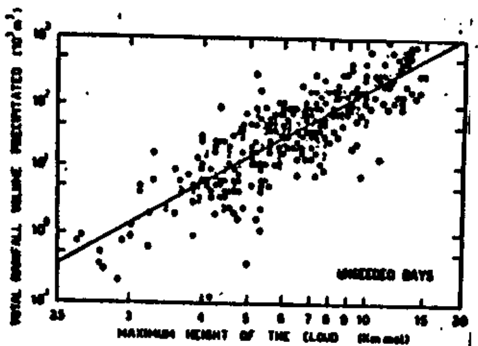


FIG. 9. As in Fig. 5 but for the lifetime total rainfall volume precipitated by the cells RV and $H_{max} - h$.

evident in the newer updraft indicating stronger upward mass transport from below. Also evident at this level is the relative inflow along the flank of the parent cell. This suggests that the parent updraft is beginning to decay.

By one hour, the dominant upward motion at the surface was positioned to the east and slightly north of the downdraft region. This updraft appears to be

original circulation (see Fig. 14b) in the northern quadrant of the storm. By 50 min, the older updraft had become disconnected from the moist, low-level air and subsequently weakened, eventually turning into a downdraft throughout the region.

for experiment B.

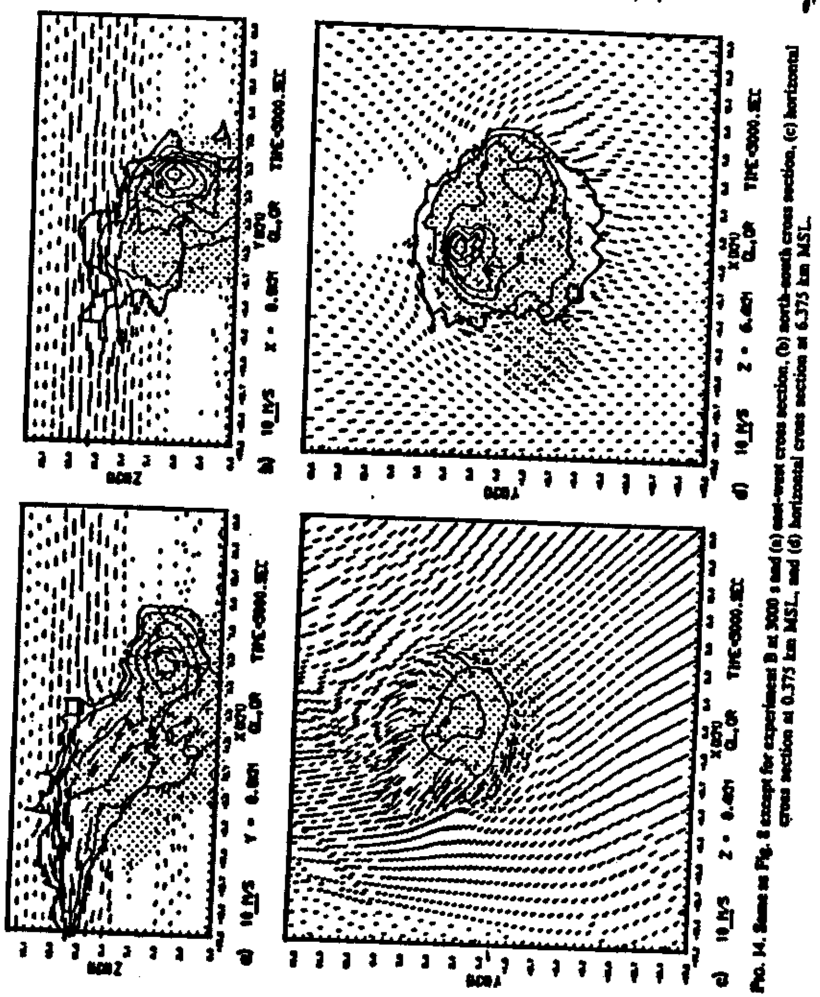

FIG. 14. Same as Fig. 8 except for experiment B at 3000 s and (a) east-west cross section, (b) north-south cross section, (c) horizontal cross section at 0.375 km MSL, and (d) horizontal cross section at 6.375 km MSL.

tions A–E.

to the LCL as well as the new updraft can be seen in f the simulated storm (see updraft associated with the

WOODLEY et al. 1982
J. Appl. Meteor., p.139

**TABLE 6.1. Summary of hypothesized dynamic seeding chain of events***

**Stage I: Initial vertical tower growth**

1. Rapid glaciation of the updraft regions of supercooled convective tower(s) by silver iodide pyrotechnic seeding.
2. Invigoration of the updrafts through buoyancy increase produced by the release of latent heats of fusion and perhaps deposition; the latter may or may not contribute as the cloud air approaches saturation relative to ice.
3. Pressure falls beneath the actively growing tower due to upward acceleration and upper level warming followed by increased inflow at mid to low levels (surface to 6 km) which fuels the initial stage of cloud growth.

Stage I may last 10-20 min, sometimes longer.

**Stage II: Horizontal cloud expansion, secondary growth**

4. Enhanced downdrafts below the invigorated seeded tower as the precipitation and evaporatively cooled air moves downward.
5. Convergence at the interface between the downdraft and the ambient low-level flow, instigating tower ascent fed by the warm, moist inflow.
6. Growth of secondary towers (which, in turn, might be seeded).
7. Horizontal enlargement of the cloud by joining of the feeder towers, leading to wider protected updraft(s), augmented condensation, water content, rainfall.

Stage II may last 30-60 min.

**Stage III: Interaction with neighboring clouds**

8. Seeding of secondary towers in the parent cloud results in their growth, followed by expansion and intensification of the downdraft area which then moves outward to interact with outflows from neighboring clouds (which might also have been seeded). This increases the convergence on a larger scale, deepens the moist layer and results in new cloud growth and merger in the convergent regions between the cloud systems. These new towers are normally seeded as well.
9. The increased seeding-induced growth and merger of clouds on the mesoscale coupled with sinking in their near environments results in a mesoscale region of warming (~50 km on a side). The resulting thermally direct mesoscale circulation provides additional low-level mass and moisture convergence to fuel new cloud development and perhaps to prolong the lives of the older cloud systems. Further, under certain conditions, the upward branch of the mesoscale circulations may become saturated and produce a period of stable (non-convective) rainfall.

**Stage IV: Increased area rainfall**

10. Seeding increases rainfall over the floating target by:
    a. enhancing the growth of the directly treated cloud towers,
    b. inducing additional cloud growth and larger cloud systems through the mechanism of downdraft interactions,
    c. indirectly increasing the efficiency of cloud elements as they grow in the more moist environment provided by the larger cloud systems; and
    d. augmenting the supply of available moisture through the enhancement of the thermally-direct mesoscale circulation.
11. Seeding increases rainfall over the total target by:
    a. obtaining more rain from the available moisture than would have occurred naturally, and/or by
    b. enhancing the moisture supply to the target.



GAGIN 1986
Met. Monogr. 21/43

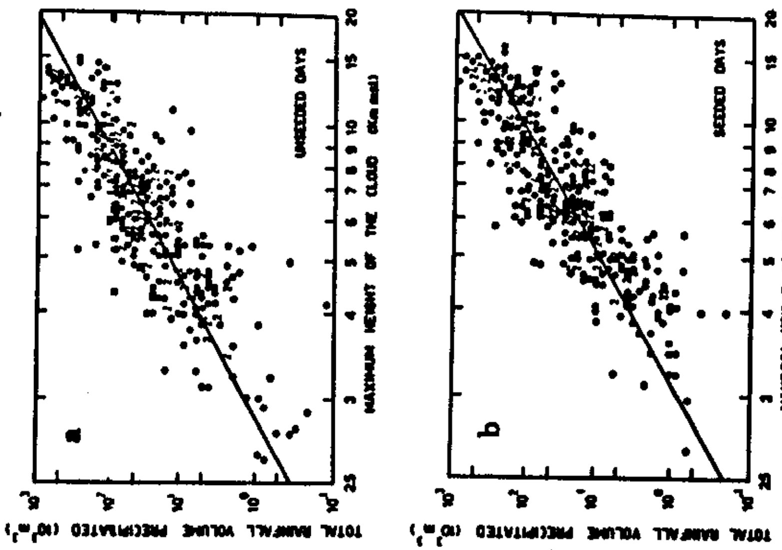


FIG. 7.4. The relationship between the lifetime total rainfall volume precipitated by the cells, RV, and the factor ($H_{max}$–h) defined by the lifetime maximum height, $H_{max}$, of the cells. (a) Relates to cells on unseeded days (unseeded) and (b) to cells on AgI-treated days (seeded).

SIMPSON et al. 1967
J. Appl. Meteor., p 82

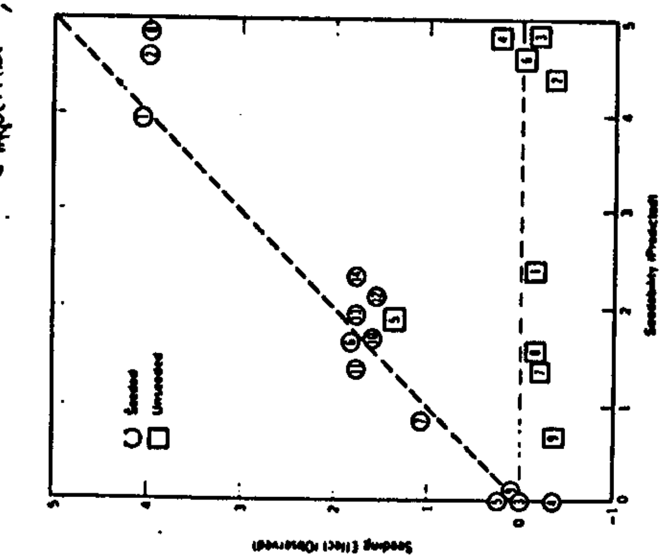


FIG. 6.3. Seedability versus seeding effect for the 14 seeded (circles) and 9 control (squares) clouds studied in 1965. Note that seeded clouds lie mainly along a straight line with slope 1 (seeding effect is close to seedability), while control clouds lie mainly along a straight horizontal line (showing little or no seeding effect regardless of magnitude of seedability). Units of each axis are in kilometers. (From Simpson et al., 1967.)

from "Hailstorms of the High Plains"

## Aircraft observation of inflow structure

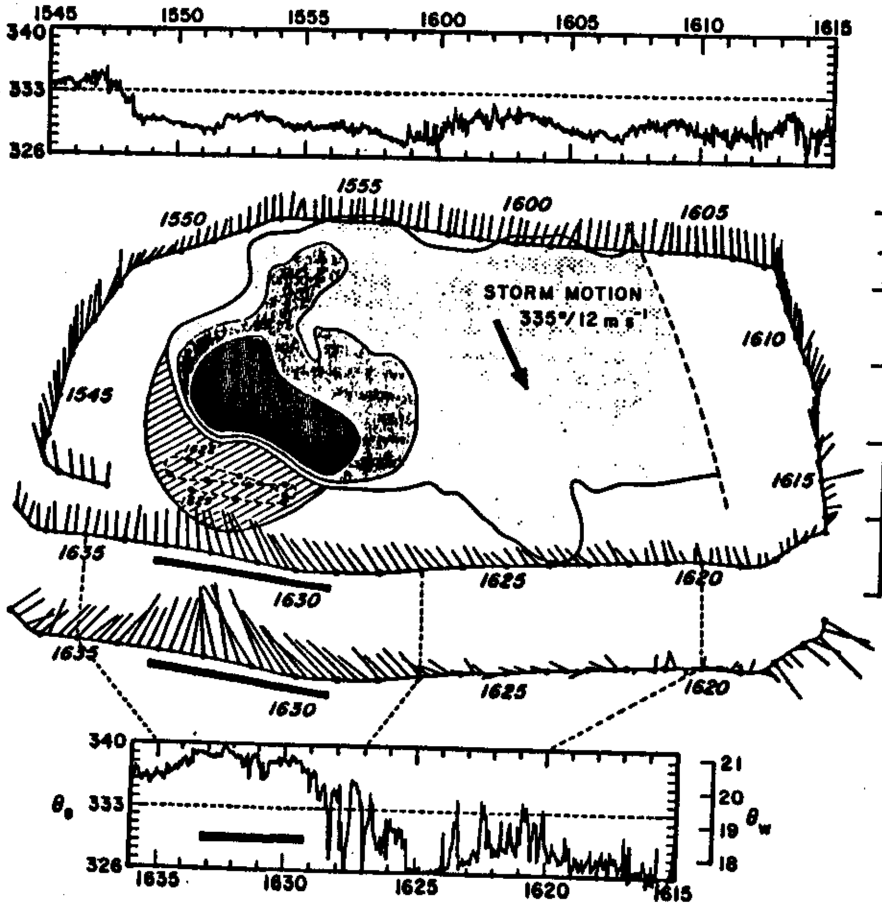


Figure 6.33 Track of aircraft flying at 2.3 km (MSL) plotted relative to storm indicated by interior radar intensity contours, with horizontal wind vectors relative to the storm plotted at 15-s intervals along the track. The offset track segment displays winds with respect to the ground (note different vector scale on the left). Dashed segment shows portion of a second aircraft track flown near cloud base in the main updraft beneath extensive echo overhang denoted by cross-hatching. Bold bar designates region of ascent along outer flight track. Panels at the top and bottom give equivalent potential temperature in the outflow and inflow sectors, respectively. A striking feature is the horizontal confluence measured across the inflow upwind of the primary updraft zone (after Browning and Foote, 1976).



UPDRAFT STATISTICS
NEAR −5°C LEVEL ; 10kW

$\bar{w} > 3$ m s⁻¹ over 1 km
all $w_i > 2$ m s⁻¹

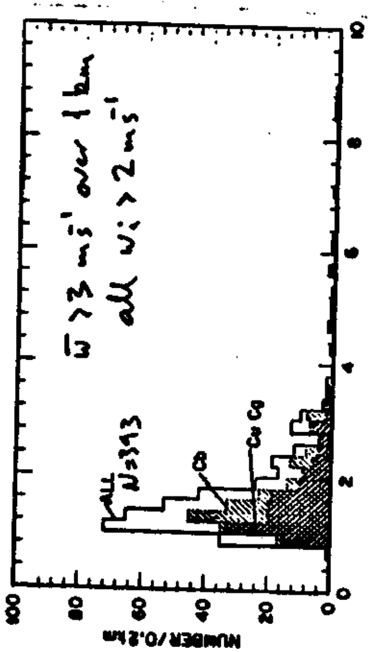


Figure 6.47 Number frequency (per 0.4-km class interval) of the horizontal dimension of updrafts observed near cloud base altitude on 22 storm days in 1976. Distributions for cumulus congestus (double hatched), cumulonimbus (single hatched), and all clouds are presented.

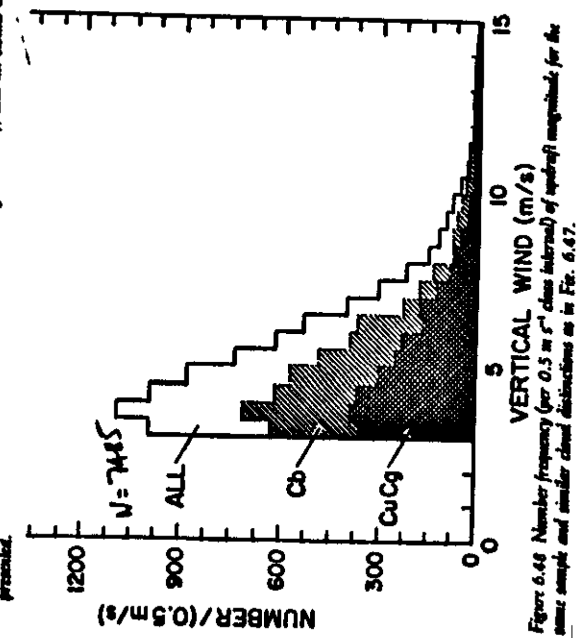


Figure 6.48 Number frequency (per 0.5 m s⁻¹ class interval) of updraft magnitude for the same sample and similar cloud distinctions as in Fig. 6.47.

W REGIONS OF LWC

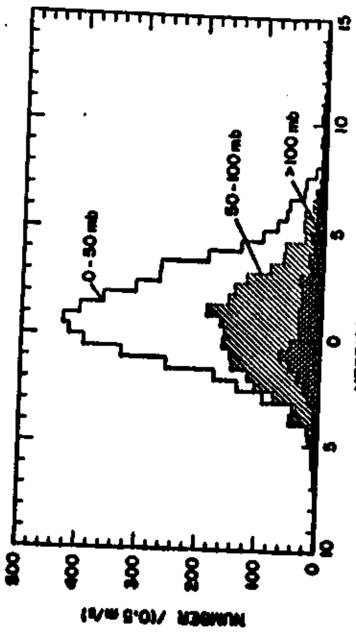


Figure 6.49 Number frequency (per 0.5 m s⁻¹ class interval) of vertical velocity in regions of significant cloud water concentration. Single hatching indicates measurements within 50 to 100 mb of cloud base, no hatching those made within 50 mb of cloud base, and double hatching those more than 100 mb from cloud base.

# SAILPLANE OBS. IN UPDRAFTS

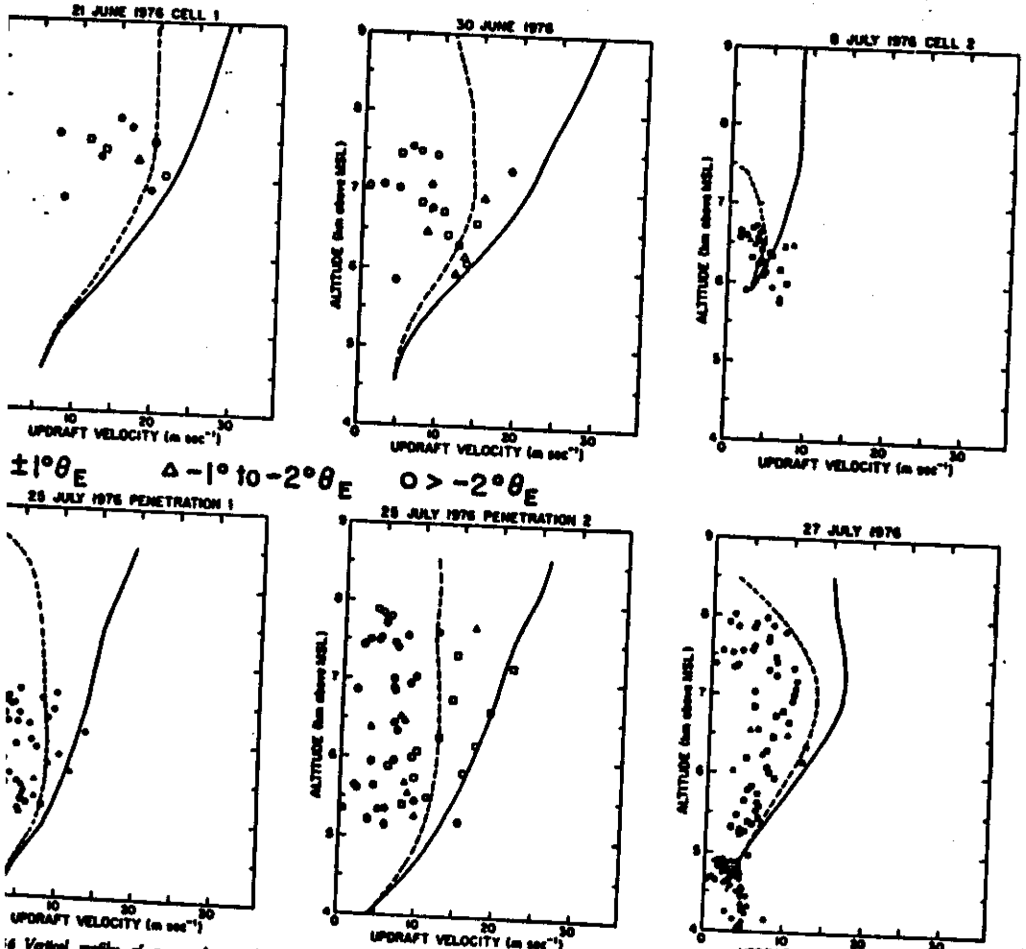


...6 Vertical profiles of measured vertical velocities from the sailplane ...ts for six clouds investigated in detail. Solid lines: vertical velocity predicted ...dimensional adiabatic parcel model; dashed lines: vertical velocity predicted from lateral entrainment theory using an entrainment coefficient of 0.1. Symbols represent departure of $\theta_e$ from cloud-base value (after Heymsfield et al., 1978).



# LWC NEAR CLOUD BASE

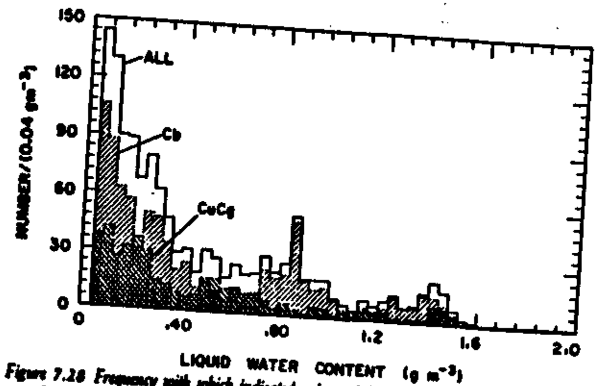


*Figure 7.28* Frequency with which indicated values of the liquid water content were observed. There were 1264 measurements in the total data set (from July only), of which 866 were Cb and 423 were CuCg measurements. When normalized, all the distributions are similar except for an excess of Cb values near 0.8 g m$^{-3}$.

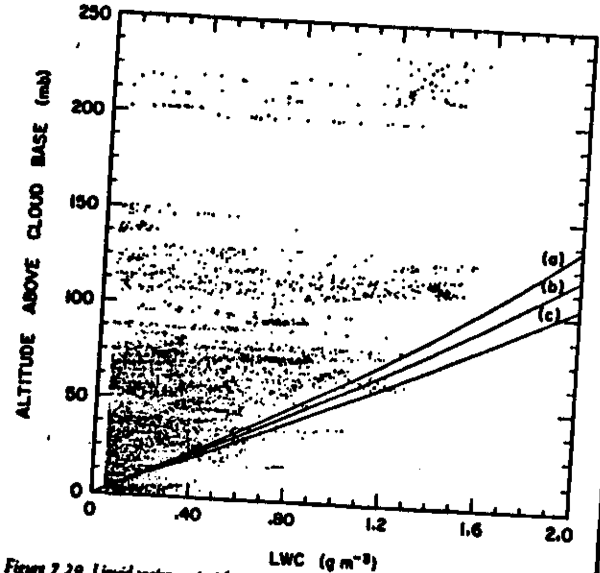


*Figure 7.29* Liquid water content (measured by the J-W probe) plotted against the altitude above cloud base. The three lines indicate the adiabatic liquid water content for cloud base conditions of (a) 602 mb, 1.5°C; (b) 650 mb, 5.0°C; and (c) 752 mb, 11.0°C. This set of values brackets the range of cloud base conditions that were present during these studies. There are 5328 points, each representing a 1-s measurement.

LIQUID WATER CONTENT
COMPARED TO ADIABATIC VALUE

-5°C LEVEL

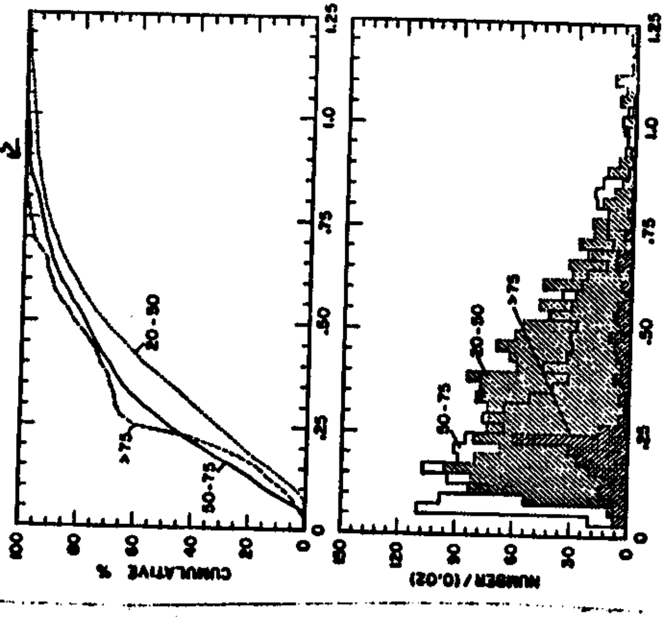


Figure 7.31 The cumulative (above) and differential (below) frequencies of occurrence of various fractions of the adiabatic liquid water content. There are three different categories, stratified according to the height in mb above cloud base. There were 1755 measurements made 20-50 mb above cloud base, 1586 made 50-75 mb above cloud base, and 312 made more than 75 mb above cloud base.

SAILPLANE

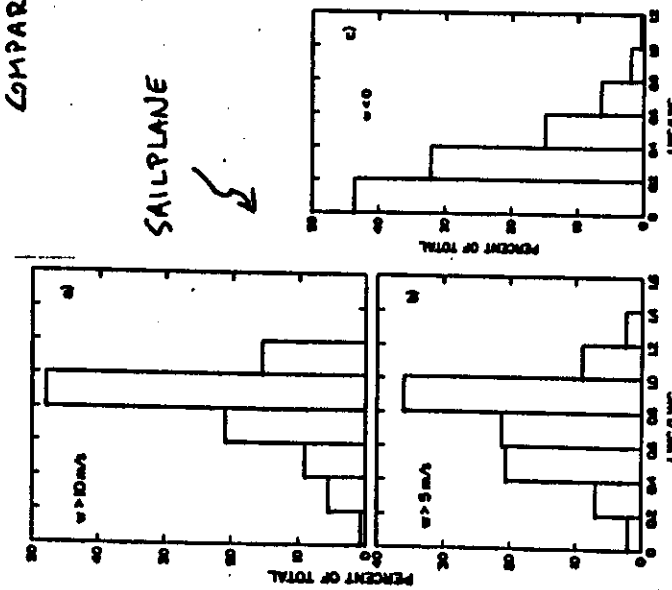


Figure 7.19 The frequency of occurrence of different ranges of percentage of adiabatic liquid water content (LWC/LWC$_A$) are presented for two updraft strengths (a) and (b) and for downdrafts (c). The data are combined from four long ascents, 22 June and 6, 22, and 23 July, though the portion of the 6 July case in which dry entrainment was an important effect is not included.



LWC
SUMMARY

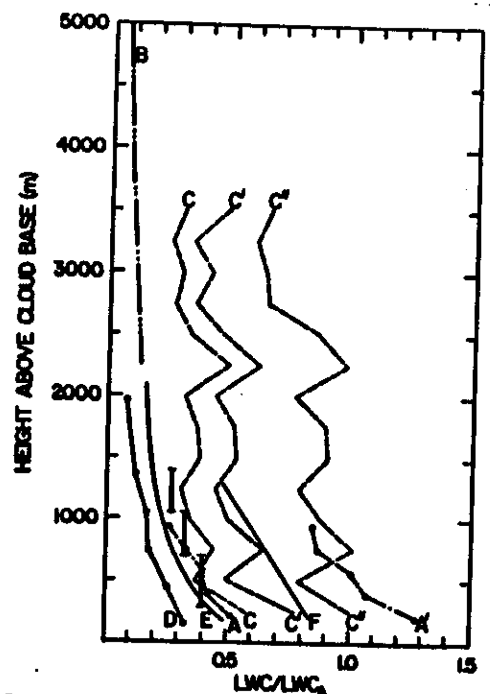


Figure 6.59 The ratio of the observed mean liquid water content at a given height above cloud base to the adiabatic value. The Wyoming Queen Air data indicated by the solid vertical lines have been superimposed on a plot of other measurements summarized in Table 6.4. The length of the vertical lines represent the altitude intervals over which the Wyoming Queen Air data have been averaged.

**TABLE 6.4**
**Summary of data relating to curves in Fig. 6.59**

| Curve | Reference | Type of cloud | Quantity plotted | Quantity averaged |
|---|---|---|---|---|
| A | Ackerman, 1959 | tropical cumuli (Bahamas) | LWC/LWC$_A$ | penetration mean |
| A' | Ackerman, 1959 | tropical cumuli (Bahamas) | LWC$_{max}$/LWC$_A$ | maximum per penetration |
| B | Ackerman, 1963 | hurricanes | LWC/LWC$_A$ | penetration mean |
| C | Skatskii, 1965 | small cumuli and mature thunderstorms mainly continental (USSR) | LWC/LWC$_A$* | penetration mean |
| C' | Skatskii, 1965 | small cumuli and mature thunderstorms mainly continental (USSR) | LWC$_{up}$/LWC$_A$* | updraft mean |
| C'' | Skatskii, 1965 | small cumuli and mature thunderstorms mainly continental (USSR) | LWC$_{max}$/LWC$_A$* | maximum per penetration |
| D | Squires, 1958 | nonprecipitating small tropical cumuli (Australia) | LWC/LWC$_A$ | median per penetration |
| E | Warner, 1955 | nonprecipitating small tropical cumuli (Australia), about 2 km deep | LWC/LWC$_A$ | mean value in the higher liquid water regions |
| F | Breed, 1979 | small continental cumuli, mostly nonprecipitating (Colorado mountains) | LWC/LWC$_A$ | penetration mean, predominantly in updrafts, as measured in sailplane ascents |
| Solid bars | present data | continental cumuli in N.E. Colorado plains, 3-8 km deep | LWC/LWC$_A$ | 1-s (~80 m) data stratified according to altitude above cloud base |

*LWC$_A$ was computed assuming median cloud base conditions 840 mb, +8°C.

EVIDENCE FOR CLOUD-TOP ENTRAINMENT

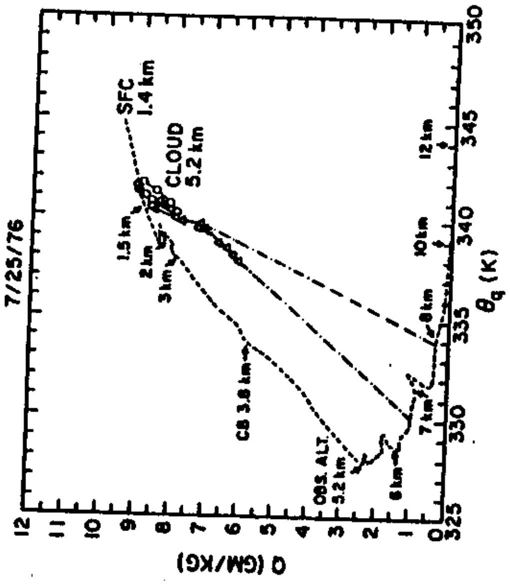


Figure 6.62b As in (a) except later in the flight. Cloud air with the observed properties could have been formed by mixing air from the surface levels with air from about 6.5 to 8 km. The observation level was 5.2 km.

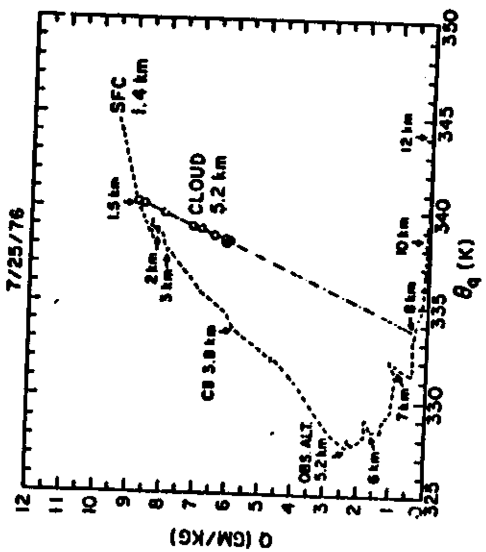


Figure 6.62a Comparisons of the total mixing ratio Q and the wet equivalent potential temperature $\theta_q$ computed from data collected inside a growing cumulus cloud with Q and $\theta_q$ values of a representative sounding. The dashed line refers to the sounding, the arrows indicate sounding altitude (MSL), and the points connected by lines represent sailplane in-cloud observations. Air with the observed properties could have been formed by mixing air from the surface levels with air from ≈9 km, as indicated by the dot-dashed line. The observation level was 5.2 km (−2°C). Cloud base (CB) was at 3.8 km (after Paluch, 1979).



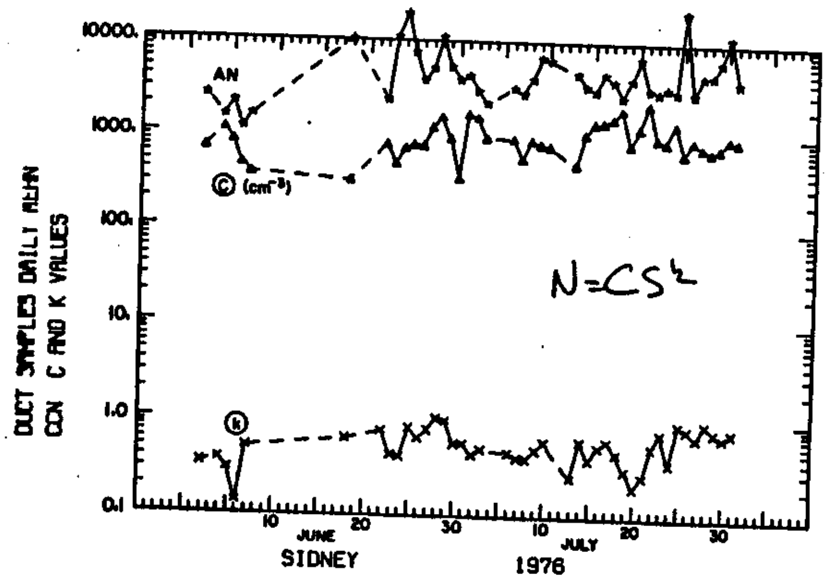


CCN MEASUREM. AT SFC.

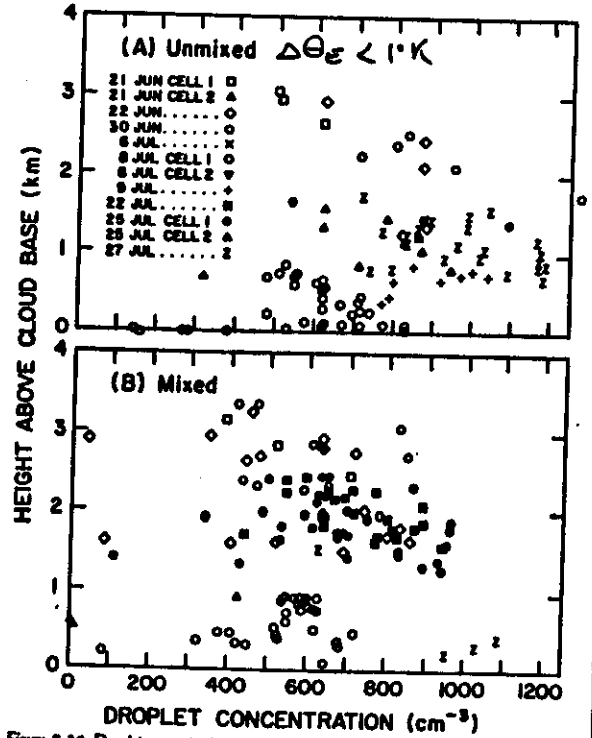


Figure 7.20 Droplet concentrations from sailplane FSSP data, 10-s averages, as a function of height above cloud base.

CLOUD DROPLET CONC. ALOFT

10 UW

$\bar{w} > 3\ m\ s^{-1}$
$N_L > 20\ cm^{-3}$
50 CASES
~ −5°C

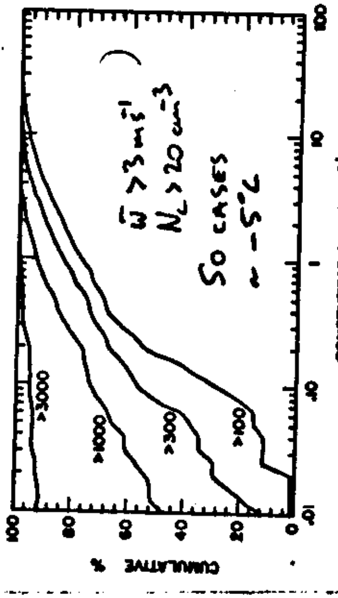

Figure 7.38 The cumulative percentage of all measurements of ice crystal concentration that did not exceed the indicated concentration, for various minimum sizes (labeled in μm). The data are from the overlap between cloud water and updraft region. There are 2336 measurements.

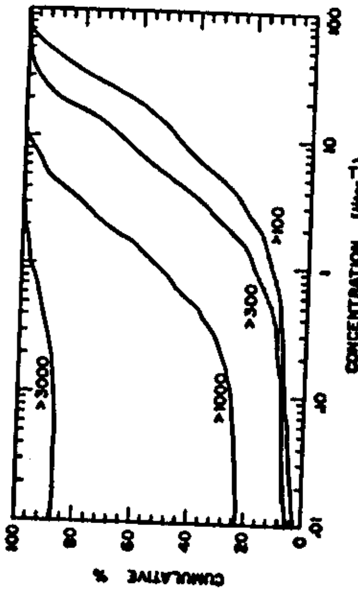

Figure 7.39 As in Fig. 7.38, for downdraft regions.

ICE CRYSTAL OBS.

SAILPLANE

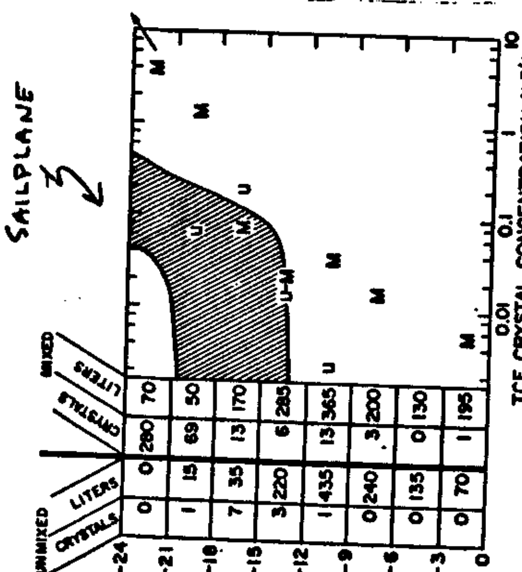

Figure 7.43 Ice crystal concentrations in unmixed (U,I) and mixed (M) portions of updraft, as measured from the sailplane. Ice is restricted to diameters between 100 and 200 μm, and unmixed is defined as having $\theta_e$ within 1 K of the cloud base value. The shaded area shows the range of expected concentrations calculated from ice nucleus measurements, and the raw data are given at the left. (From Heymsfield et al., 1979.)



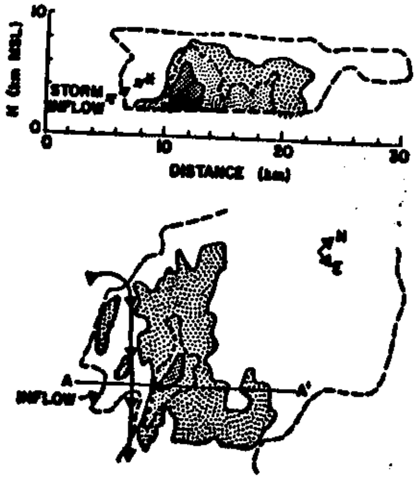

*Figure 8. A moderate rainshower in the Miles City HIPLEX area. Top: vertical cross-section showing the radar structure of the storm. The asterisk shows the position of the aircraft penetration. The vertical wind was 10 m/s and the horizontal wind was 20 m/s at this point. The reflectivity contours are in 10 dBz increments beginning at 10 dBz; maximum radar reflectivity was about 46 dBz. Bottom: a PPI plot of the same through the altitude of the aircraft. The flight track is indicated by the line with arrows, and the line A-A' shows the line along which the vertical section in the top half of the figure was constructed.*

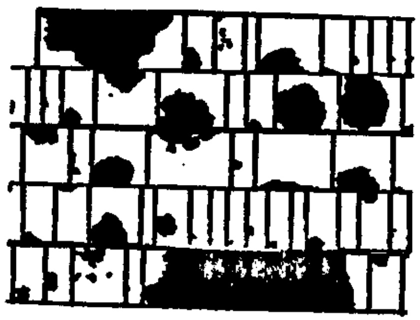

*Figure 9. 2-D images representative of the*

The later stages of the same storm discussed in section 3 provide another example of a severe storm. By this time, hail was present in the storm and was falling from the base. We did not penetrate the region of high reflectivity, which reached 50 dBz at this time, but rather skirted the side of this region. The radar

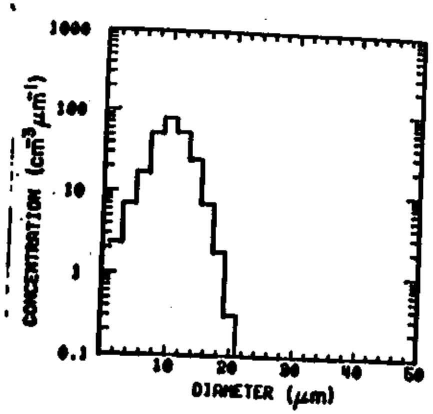

*Figure 10. The cloud droplet spectrum measured during the pass shown in Fig. 8. The droplet concentration is 486 cm⁻³, and the liquid water content is 0.33 g m⁻³.*

*Figure 11. 2-D images from the inflow region of the storm of 8 July 1977.*

structure of the storm at this time, which was about 30 min after the first echo, is shown in Fig. 12. The strongest inflow to the storm was on the south side, and new turret development was on the southwest corner of the storm. Fig. 12 shows two aircraft passes through this storm, and Fig. 13 shows some examples of the 2-D images from the edges of the precipitation core. One of these images is a 7 mm hailstone, and several others are in excess of 4 mm diameter. Again, no images consistent with rain images were found, and the shape of the cloud droplet spectrum remained similar to that shown in Fig. 4.

Although the observed precipitation in all of these studies was graupel, the precipitation mechanism cannot be inferred with as much confidence in these severe storms. A large portion of the storms extended to altitudes well above the flight level, and much of the precipitation formed at these high levels. Furthermore, it was common to find the strongest inflow regions devoid of any precipitation embryos, either ice or water. If a coalescence process operates in these storms, the rain must be soon converted to graupel because no rain drops were observed.

HIPLEX, MONTANA EXP.

-12 to -15°C

+3°C
2-2.5 km

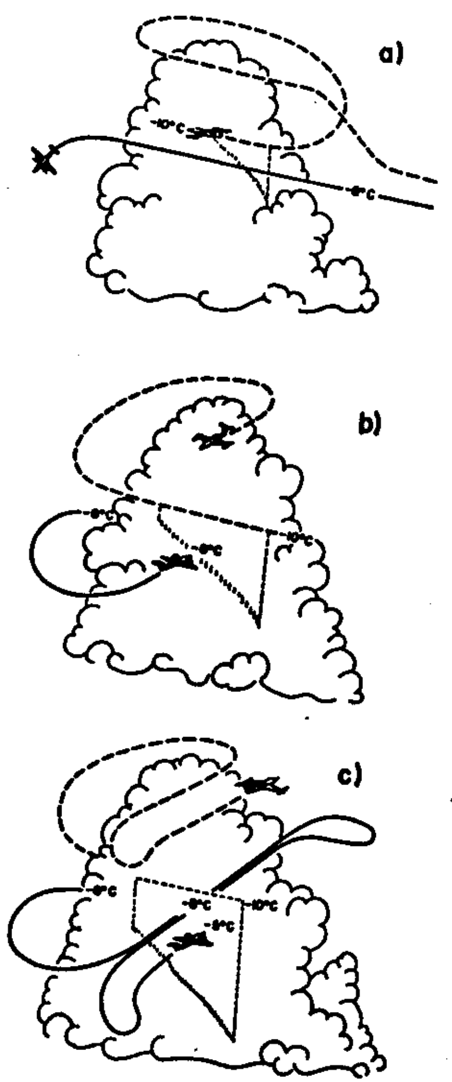


Fig. 4.1: Scenario of the sequential (frames a-c) HIPLEX-1 flight procedures followed by the CIC Learjet and the University of Wyoming Super King Air aircraft. Further explanation is found in the text.



HIPLEX RESULTS

IV/2

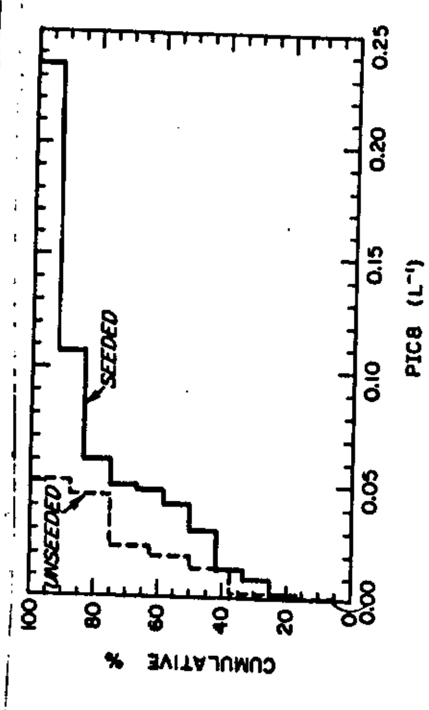


Fig. 4.8: Cumulative distributions for the response variable PIC8, representing the concentration of precipitating ice hydrometeors (at least 600 µm in longest dimension) in the HIPLEX-1 clouds 8 min after treatment.

IV/24

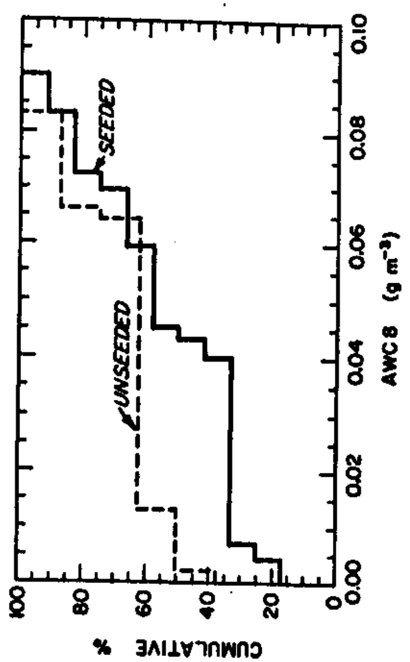


Fig. 4.11: Cumulative distributions for the response variable AWC8, representing the 4-km average liquid water content 8 min after treatment of the HIPLEX-1 clouds.

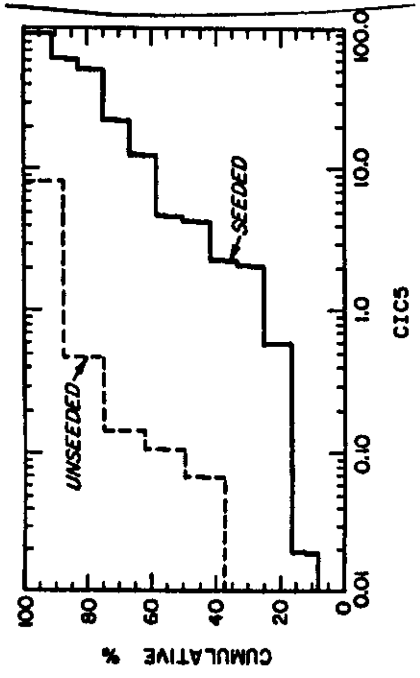


. 4.3: Cumulative distributions for the response variable CIC5, ...senting the ice concentration 5 min after treatment of the ...EX-1 clouds.

IV/25

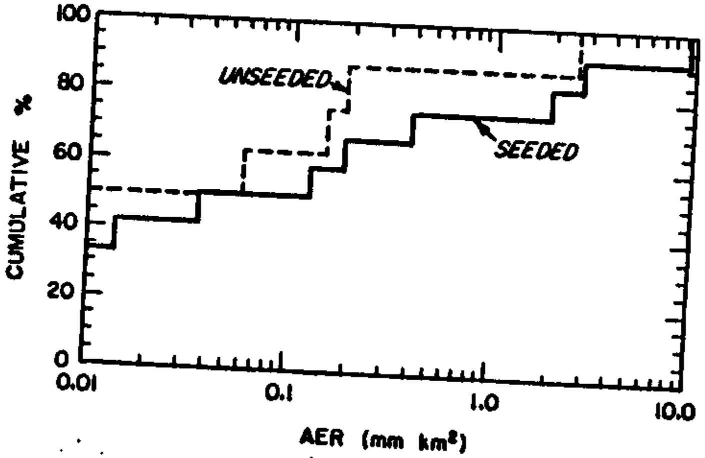


**Fig. 4.15:** Cumulative distributions for the HIPLEX-1 response variable AER, representing the aircraft-estimated rainfall from each of the HIPLEX-1 clouds.

IV/

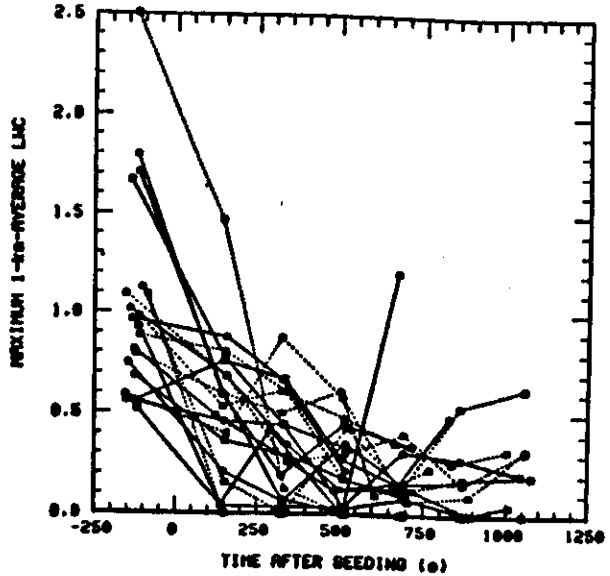


**Fig. 4.16:** The maximum 1-km average liquid water content encountered on each pass through HIPLEX-1 clouds, as a function of time after treatment. Points from the same cloud are connected, by solid lines for seeded and by dashed lines for unseeded clouds.

LWC vs. GRAUPEL GROWTH TIME (CALC.)

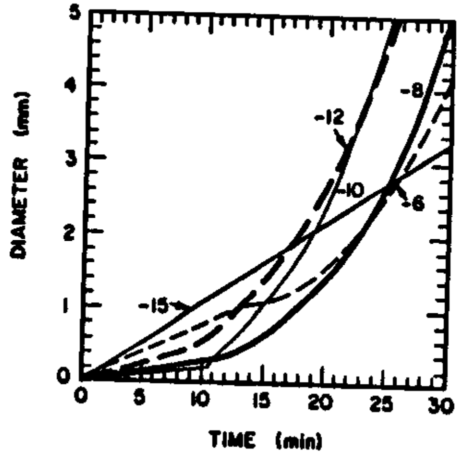


**Fig. 3.17:** Graupel particle diameter as a function of time for the various indicated temperatures. All calculations were for a pressure of 500 mb, a liquid water content of 1 $g/m^3$, and a cloud droplet diameter of 20 µm.